ARTICLE

Photoactive Hybrid Nanomaterials: Indocyanine Immobilized in Mesoporous MCM-41 for "In-Cell" Bioimaging

Enrica Gianotti,*,† Chiara A. Bertolino,†,‡ Caterina Benzi,† Giuseppina Nicotra,§ Giuseppe Caputo,†,‡ Roberta Castino,§ Ciro Isidoro,§,|| and Salvatore Coluccia†

Dipartimento di Chimica IFM and NIS Centre of Excellence, Università di Torino, Via P. Giuria 7, 10125 Torino, Italy, Cyanine Technologies S.r.l., Via Quarello 11/13, 10138 Torino, Italy, Laboratory of Molecular Pathology and Nanobioimaging, Dipartimento di Scienze Mediche, Università del Piemonte Orientale "A. Avogadro", Via P. Solaroli 17, 28100 Novara, Italy, and Centro NanoSistemi, Alessandria, Italy

ABSTRACT Mesoporous silica nanoparticles are being explored as versatile tools for various biomedical and biotechnological applications including disease diagnosis, drug delivery, and intracellular imaging. In this paper, the synthesis and characterization of a fluorescent hybrid mesoporous silica nanomaterial, which is noncytotoxic and shows great potential for "in-cell" bioimaging applications, will be described. The hybrid mesoporous material has been obtained by confining highly fluorescent organic dyes, belonging to the indocyanine family, within the channels of mesoporous MCM-41. To explore the dispersion of the dye inside the mesoporous channels and the formation of dye aggregates, several hybrid samples with increasing dye/MCM-41 loading (up to 100 mg/g) were prepared. A uniform distribution of monomeric 1,1′-diethyl-3,3,3′,3′-tetramethylindocarbocyanine iodide has been achieved at low dye loading (1 mg/g), as evidenced by photoluminescence spectra and lifetime, while a progressive formation of *J*-aggregates is induced by an increase in the dye loading. To elucidate the properties of the dye immobilized in mesoporous MCM-41, a detailed physical chemical characterization by structural (X-ray diffraction), volumetric and optical (Fourier transform infrared, diffuse-reflectance UV−vis and photoluminescence) techniques has been performed. By ultrasonication of the bulk material, nanoparticles of 2−20 nm diameter were obtained. Biocompatibility, endocytic uptake, and intracellular compartmentalization of such fluorescent nanoparticles were investigated in mammalian cultured cells.

KEYWORDS: indocyanine • MCM-41 • hybrid materials • photoactive nanoparticles • bioimaging • lysosomes

1. INTRODUCTION

Both porous and solid silica nanoparticles (NPs) conjugated with photoactive dyes have been proven to be excellent highly sensitive molecular probes for biomedical and biotechnological applications such as imaging of cellular processes, genomic and proteomic analyses, and clinical diagnostics (1−3).

Ordered nanostructured porous materials are attracting increasing attention because their synthesis allows precise control of the features and morphology. Recently, these materials have been exploited as hosts for organic dyes to produce a new class of hybrid materials with potential application in solid lasers (4), photoinduced switching (5), optical sensors (6), and cellular imaging (7). In particular, silica mesoporous NPs doped with fluorescent dyes have the potential to track by optical imaging a variety of biological processes, such as cellular uptake of drugs, vesicular traffic, cell migration, cell proliferation, and cell death. Several kinds of fluorescent organic dyes (coumarins (8−11), fluoresceins (12), porphyrins (13), rhodamines (14), thionines (15), cyanines (16, 17), etc.), confined within mesoporous siliceous materials such as MCM-41 (12), MCM-48 (10), and SBA-15 (17), have been investigated. Among organic fluorophores, indocyanine dyes are particularly attractive as guest dyes within mesoporous materials. Indocyanine dyes are of utmost importance in the fields of molecular diagnostics and life sciences (18−20) thanks to their strong fluorescence, which enables the dyes to detect labeled compounds at trace levels. Moreover, the absorption and emission performance of cyanine dyes (emission range from 500 to 900 nm) can be tuned toward near-infrared by structural modifications (21). The emission in the near-infrared region is particularly important for "in-cell" imaging because in this spectral region the self-emission (i.e., autofluorescence) of biomolecules and tissues is at a minimum. In the last 10 years, novel cyanine dyes were synthesized by our group, improving both the stability and optical performance (22−24). In particular, 1,1′-diethyl-3,3,3′,3′-tetramethylindocarbocyanine iodide (IRIS3) is an ideal model of a cationic cyanine dye and shows an intense absorption (extinction coefficient $\sim 110\,000\ M^{-1}\ cm^{-1}$) and emission (quantum efficiency ~ 0.15) in the visible (absorption max = 545 nm, emission max = 564 nm in methanol) spectrum; it has good solubility in organic solvents and is photostable in solution for several

* To whom correspondence should be addressed. Tel.: +39 011 6705344. Fax: +30 011 6707953. E-mail: enrica.gianotti@unito.it.

Received for review November 26, 2008 and accepted February 11, 2009

† Università di Torino.

‡ Cyanine Technologies srl.

§ Università del Piemonte Orientale "A. Avogadro".

|| Centro NanoSistemi.

DOI: 10.1021/am800196r

Published on Web 03/09/2009

Scheme 1. IRIS3 Structure

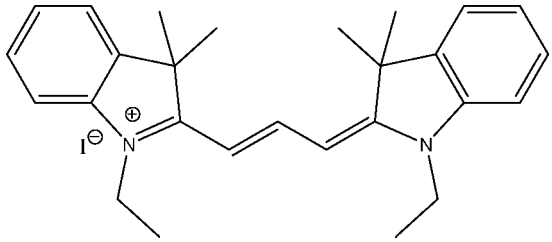

days (25). IRIS3 has a quasi-planar structure (Scheme 1), with the alkyl groups out of the plane, and its dimensions are about 5 × 14 Å (25), which allows the molecule to be included within the hexagonal channels of mesoporous materials.

The confinement of a dye into the channels of mesoporous systems has some important advantages including the protection of the dye molecules against chemical attack, photobleaching, and thermal decomposition (26). The uniform and adjustable environment of nanostructured mesoporous siliceous materials, such as MCM-41, leads to a homogeneous distribution of the organic molecules, which can be achieved by impregnation (10), grafting (14), or one-pot synthesis (12).

The unique structure of mesoporous silicas allows them to host in their internal channels not only molecular imaging agents but also drugs and biomolecules (e.g., peptides and nucleic acids) contemporaneiously (27−29). Moreover, the channels of mesoporous silicas can be opened or closed by different systems sensitive to specific triggers (e.g., pH, light, and heat), thus allowing a controlled release of the guest molecule (30). The possibility of coupling optical imaging with drug delivery (and its controlled release) justifies the broad interest in developing these hybrid mesoporous materials for biological and medical applications.

In the present paper, the synthesis and structural and optical characterization of as-prepared photoactive hybrid mesoporous materials based on the immobilization of IRIS3 in mesoporous MCM-41 will be described. Hybrid materials with increasing dye/MCM-41 ratios were explored to elucidate the changes in the optical properties of the dye within the mesoporous channels. All of the materials have been studied by means of X-ray diffraction (XRD), high-resolution transmission electron microscopy (HRTEM), dynamic light scattering, thermogravimetric and volumetric analyses, and diffuse-reflectance (DR) UV−vis and photoluminescence spectroscopies. The application of these photoactive systems to intracellular imaging is possible if the particle sizes are in the nanometric range. For this purpose, the bulk material was sonicated to produce 2−20 nm NPs, which were then characterized for their photochemical properties and biocompatibility in cell cultures.

2. MATERIALS AND METHODS

2.1. Synthesis of IRIS3. 1,1′-Diethyl-3,3,3′,3′-tetramethylindocarbocyanine iodide (IRIS3; Scheme 1) was synthesized according to the method of Hamer (31) and purified by flash chromatography (95:5 methanol in dichloromethane as the eluent). The structure was confirmed by mass spectrometry (Finnigan Mat TSQ700) and ^{1}H NMR (Bruker Avance 400 MHz, DMSO-d_6).

Table 1. Nominal and Actual IRIS3 Loading in the Hybrids

	nominal IRIS3 loading (mg/g)	actual IRIS3 loading (mg/g)
IRIS3(1)/MCM-41	1	1
IRIS3(10)/MCM-41	10	9.9
IRIS3(100)MCM-41	100	95.2

2.2. Synthesis of Photoactive Hybrids and NPs. Thermally stable siliceous mesoporous MCM-41 was synthesized according to a literature method using cetyltrimethylammonium bromide (CTMAB) as a structure-directing agent (32). The gel composition of the synthesis mixture was 1:0.27:0.19:40 SiO_2 (Aerosil)/CTMAB/TMAOH/H_2O. CTMAB surfactant was removed from the as-synthesized material at 550 °C, first under a N_2 flow and subsequently under O_2. The resultant dried MCM-41 was stored under ambient conditions. MCM-41 was outgassed at 150 °C for 4 h to remove the adsorbed water and then impregnated with solutions of IRIS3 in anhydrous toluene. The mixture was stirred for 2 h at room temperature, under a N_2 atmosphere. The solid hybrid was filtered and dried under vacuum. The leaching of the dye was analyzed by mixing 50 mg of hybrid with 10 mL of anhydrous toluene and stirring for 30 min at room temperature. After centrifugation (20 min at 6000 rpm) and filtration, the IRIS3 concentration in the supernatant was analyzed by UV−vis spectrophotometer (IRIS3: $\epsilon_{561\ nm} = 110000\ M^{-1}\ cm^{-1}$ in toluene, measured from the slope of a Lambert−Beer plot) (26). Three hybrid materials were prepared with an increase in the IRIS3 loading in the range of 1−100 mg/g; for each hybrid, the UV−vis analysis of the toluene solution revealed that no free dye is present and that the actual dye loading is very close to the nominal one (Table 1). The color of the solids turns from pale to deep fuchsia depending on the IRIS3 loading. The resulting samples will be addressed as IRIS3(1)/MCM-41, IRIS3(10)/MCM-41, and IRIS3(100)/MCM-41.

To reduce the particle dimensions of photoactive hybrids for the in vitro applications, an ultrasonication treatment was applied, using an ultrasonic horn (Microson Ultrasonic Homogenizer XL2000, Misonix, Inc., Farmingdale, NY). The hybrid mesoporous powder was resuspended in distilled water (1 %) in a 1 mL Eppendorf tube. Ultrasonication was performed on ice by three cycles of 15 s at 22.5 kHz and 5 W.

2.3. Physicochemical Characterization of Photoactive Hybrids and NPs. Specific surface areas (SSAs) were measured by N_2 adsorption−desorption isotherms at 77 K using a Micromeritics ASAP 2020. The SSA was calculated by the Brunauer−Emmett−Teller method, and the average pore size was calculated on the adsorption branch of the isotherms using the Barrett−Joyner−Helenda method.

XRD patterns of MCM-41 and hybrid IRIS3/MCM-41 samples were obtained by a Philips 1830 instrument operating with Co Kα radiation, generated at 20 mA and 40 kV. The unit cell parameters were calculated using the formula $a = 2d_{100}/\sqrt{3}$, where d_{100} represents the d-spacing value of the (100) diffraction peak in XRD patterns of samples.

Fourier transform infrared (FTIR) spectra of self-supporting wafers of the samples (ca. 2 mg/cm^2) were collected with a Bruker IFS88 spectrometer at a resolution of 4 cm^{-1}. Samples were outgassed at 150 °C to remove adsorbed water before FTIR analysis.

DR UV−vis spectra were collected by a Perkin Elmer (Lambda 19) spectrometer equipped with an integrating sphere attachment. IRIS3(10)/MCM-41 and IRIS3(100)/MCM-41 were diluted in amorphous silica to avoid out-of-scaling.

Steady-state fluorescence spectra were recorded using a spectrofluorimeter (Fluorolog 3, T-format spectrometer) equipped with a sample holder for solids and with a stirrer device for analysis of the suspensions. The spectral response was corrected for the spectral sensitivity of the photomultiplier (Hamamatsu R928).

Fluorescence lifetimes were obtained by the time-correlated single-photon-counting (TCSPC) method, and the data were fitted to a multiexponential function and compared to data from the literature (33−35). Fluorescence analyses were performed at room temperature. The samples were excited by a NanoLED source (λ_{ex} = 460 nm, pulse width = 0.8−1.4 ns, and repetition rate = 1 MHz).

HRTEM was used to monitor the particle size of the hybrids after ultrasonication treatment. HRTEM measurements were performed using a JEOL 2000 EX (200 kV) electron microscope equipped with a top-entry stage and a LaB_6 filament. The NP powders were dispersed on a copper grid with a porous lacey carbon film.

A dynamic light scattering experiment was carried out on an ALV-NIBS High Performance Particle Sizer by ALV GmbH, Landen, Germany, in aqueous media.

2.4. Biocompatibility and "In-Cell" Bioimaging. The following cell lines were employed: L929 mouse fibroblasts, Rat Basophilic Leukemia (RBL)/mast cells, NIHOVCAR-3 human ovary carcinoma cells, and SH-SY5Y human neuroblastoma cells. Cell lines were obtained from ATCC (American Type Culture Collection, Manassas, VA) and cultivated under standard conditions (37 °C, 5% CO_2/air) in an appropriate medium, as previously reported (36−38). Cells plated on Petri dishes were incubated for different periods with NPs (0.01 μg/mL), and the cytoxicity was assessed as the cell loss from the monolayer, as detected by contrast phase microscopy and cell counting. The occurrence of cell death (either necrosis or apoptosis) was ascertained by vital trypan blue or propidium iodide staining and by annexin V-FITC staining, as was previously described in detail (38). For studies on cellular uptake and intracellular localization of NPs, the cells were plated on sterile coverslips. The endocytic pathway was tracked by simultaneous incubation with Lysosensor (Molecular Probes, Invitrogen Ltd., Paisley, U.K.). Endosomal−lysosomal acid compartments were labeled with acridine orange (AO; Sigma-Aldrich, St. Louis, MO) or monodansylcadaverine (MDC; Sigma-Aldrich, St. Louis, MO). In some experiments, chloroquine (CQ; Sigma-Aldrich, St. Louis, MO) was added to the culture medium to induce alkalinization of intracellular acid compartments. Lysosomal membrane permeabilization was induced by exposing the cells to 200 μM H_2O_2 for 2 h (37). Fluorescence images were captured under a Leica DMIRE2 confocal fluorescence microscope (Leica Microsystems AG, Wetzlad, Germany) equipped with Leica Confocal Software version 2.61.

3. RESULTS AND DISCUSSION

3.1. Characterization of As-Prepared Hybrid Materials. The photoactive hybrid materials were characterized by XRD and N_2 adsorption−desorption analyses to obtain information on the mesoporous structure before and after immobilization of IRIS3. The XRD analysis enables monitoring of the structural modification of MCM-41 after impregnation with cyanine dye. Figure 1 shows XRD profiles of calcined MCM-41 (curve a), IRIS3(1)/MCM-41 (curve b), IRIS3(10)/MCM-41 (curve c), and IRIS3(100)/MCM-41 (curve d). MCM-41 (curve a) shows the typical XRD pattern of an ordered hexagonal network of mesopores with (100), (110), and (200) reflections (39). The presence of well-resolved (110) and (200) peaks indicates that MCM-41, used for the preparation of hybrid materials, has a well-ordered mesopore network. The hexagonal XRD pattern was still clearly observed in all hybrid IRIS3/MCM-41 materials, as all of the three main reflections were found (curves b−d), indicating that impregnation with the dye does not affect the framework integrity of MCM-41. However, in the case of the sample with the highest loading of IRIS3 dye, IRIS3(100)/MCM-41 (curve d), the (100) peak is broadened and shifted from 2.70° (d_{100} = 38 Å) to 2.95° (d_{100} = 35 Å) together with the (110) and (200) weak signals, showing unit cell parameter a decreasing from pure MCM-41 (a = 44) to the hybrid ($a_{100\ mg/g}$ = 40).

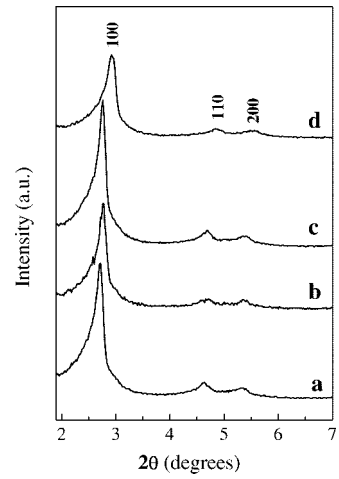

FIGURE 1. XRD patterns of calcined MCM-41 (curve a), IRIS3(1)/MCM-41 (curve b), IRIS3(10)/MCM-41 (curve c), and IRIS3(100)/MCM-41 (curve d).

N_2 adsorption−desorption isotherms of calcined MCM-41 and hybrid materials are reported in Figure 2 (left). A typical type IV isotherm is observed for all samples. The type IV isotherm with H1-type hysteresis is typical of mesoporous materials with one-dimensional cylindrical channels. The sharp inflection at 0.3−0.4 p/p_0 in the MCM-41 isotherm (curve a) corresponds to capillary condensation within uniform mesopores. The same inflection is present also in the isotherms of low dye loading samples (curves b and c), while it is in the range 0.22−0.37 p/p_0 in the high dye loading hybrid (curve d). At a pressure above 0.9 p/p_0, a hysteresis loop is observed for all samples, due to condensation in textural porosity.

The mean pore diameter and the cumulative pore volume, respectively, decrease from 2.7 nm and 0.86 cm^3/g for pure MCM-41 to 2.4 nm and 0.65 cm^3/g for the higher dye loading sample (Figure 2, right). A decrease of SSA is also observed from MCM-41 (~1000 m^2/g) to the IRIS3(100)/MCM-41 sample (~800 m^2/g). This is evidence that cyanine dyes are confined within the MCM-41 mesopores and are not just adsorbed on the external surface.

Thermogravimetric analyses performed on pure calcined MCM-41 and on hybrid materials (not reported for the sake of brevity) have evidenced that the weight loss in the 30−150 °C temperature range is due to water desorption, while at higher temperature, the weight loss is associated with dye decomposition. For this reason, FTIR spectra were

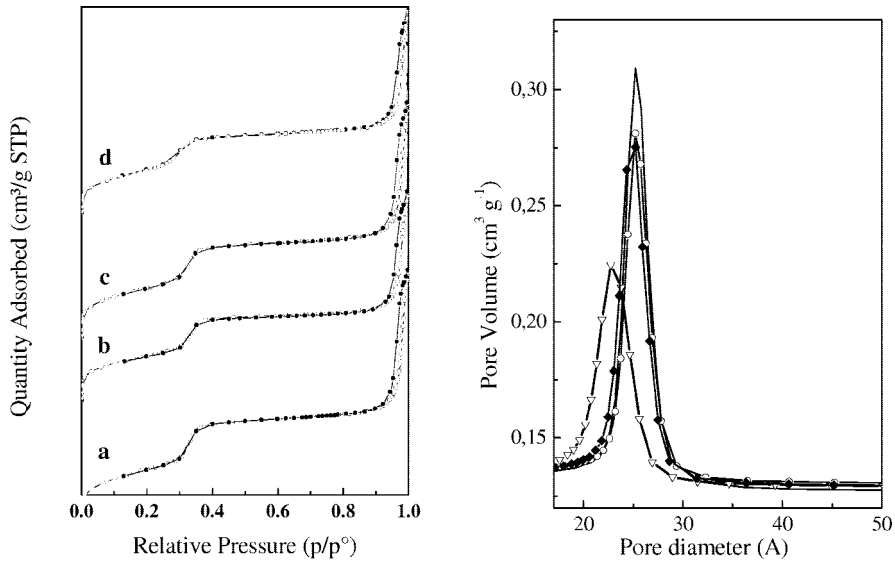

FIGURE 2. Left: N_2 adsorption (hollow symbols) and desorption (full symbols) branches of MCM-41 (curve a), IRIS3(1)/MCM-41 (curve b), IRIS3(10)/MCM-41 (curve c), and IRIS3(100)/MCM-41 (curve d). Right: Pore size distribution of MCM-41 (—), IRIS3(1)/MCM-41 (-○-), IRIS3(10)DTCI10/MCM-41 (-♦-) and IRIS3(100)/MCM-41 (-▽-).

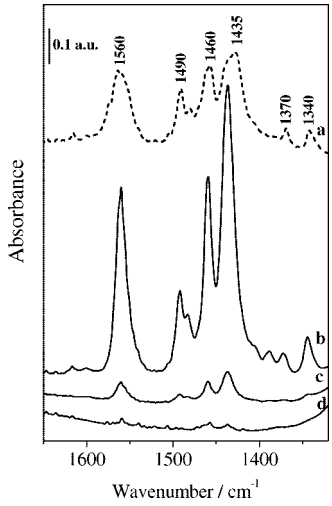

FIGURE 3. FTIR spectra of solid IRIS3 in KBr (curve a), IRIS3(100)/MCM-41 (curve b), IRIS3(10)/MCM-41 (curve c), and IRIS3(1)/MCM-41 (curve d) outgassed at 150 °C.

acquired on samples outgassed at 150 °C (residual pressure < 10^{-4} mbar), and this temperature was not exceeded to avoid thermal degradation of the dye. Figure 3 shows the FTIR spectra of the hybrid materials in the low-frequency range (1650−1300 cm^{-1}), where typical vibrational features of cyanine dyes are present. The FTIR spectrum of pure solid IRIS3 (curve a, dashed) is also reported for comparison. Pure IRIS3 shows bands that are associated with the stretching mode of C═C (1560 cm^{-1}) and C═N (1490 cm^{-1}) and with the asymmetric bending of $-CH_2$ (1435 cm^{-1}) and $-CH_3$ (1340 cm^{-1}) groups (40). The typical vibrational features of the cyanine IRIS3 are also present in the FTIR spectra of the hybrid materials, although with different intensities depending on the IRIS3 loading (curves b−d) and with different sharpness. It can be noted, in fact, that the cyanine bands are sharper in the hybrid material at highest IRIS3 loading (curve b) than in IRIS3 (curve a). However, the presence of an intact vibrational profile of IRIS3 in the hybrids confirms that the IRIS3 structure was preserved after impregnation with MCM-41.

To elucidate IRIS3 dispersion within the channels of MCM-41, the UV−vis features of the IRIS3/MCM-41 hybrids have been investigated by comparison with pure IRIS3 in solution. DR UV−vis spectra of IRIS3/MCM-41 hybrids are shown in Figure 4A. The spectra of the hybrids at increasing IRIS3 loading were compared [IRIS3(1)/MCM-41 (curve a), IRIS3(10)/MCM-41 (curve b), and IRIS3(100)/MCM-41 (curve c)] to the spectrum of IRIS3 in methanol (Figure 4B). IRIS3 in methanol was studied at a concentration of 10^{-6} M, where cyanine dye is present only in monomeric form. IRIS3(10)/MCM-41 and IRIS3(100)/MCM-41 were diluted 1:10 in SiO_2 (Aerosil); the DR UV−vis spectra of the undiluted samples were, in fact, out of scale. All intensities have been normalized at their maximum. The UV−vis spectrum of the cyanine solution (Figure 4B) shows a main absorption at 545 nm and a secondary band at 510 nm with a shoulder at 480 nm. Absorptions in the 450−575 nm range correspond to the HOMO → LUMO electron transition in the π-conjugated system. The π-conjugated system is mainly localized on the polymethine chain with a minor contribution of the indolenine rings (25). The DR UV−vis spectra of the hybrids IRIS3/MCM-41 show similar bands, although much more broadened and with different relative intensities than those in solution: an increase of the intensity of the 510 nm band is, in fact, observed. A direct comparison of the band intensity in the three hybrids is not possible because, as mentioned above, IRIS3(10) and IRIS3(100) hybrids were diluted in amorphous silica to avoid saturation of the detector. However, the broadness in the spectral profiles suggests that more species are present, although there is no evidence of any specific absorption band associated with dye aggregates. Cyanine aggregates, in fact, originate sharp absorption bands respectively at higher (*J*-aggregates) and lower (*H*-aggregates) wavelengths than the monomer and well sepa-

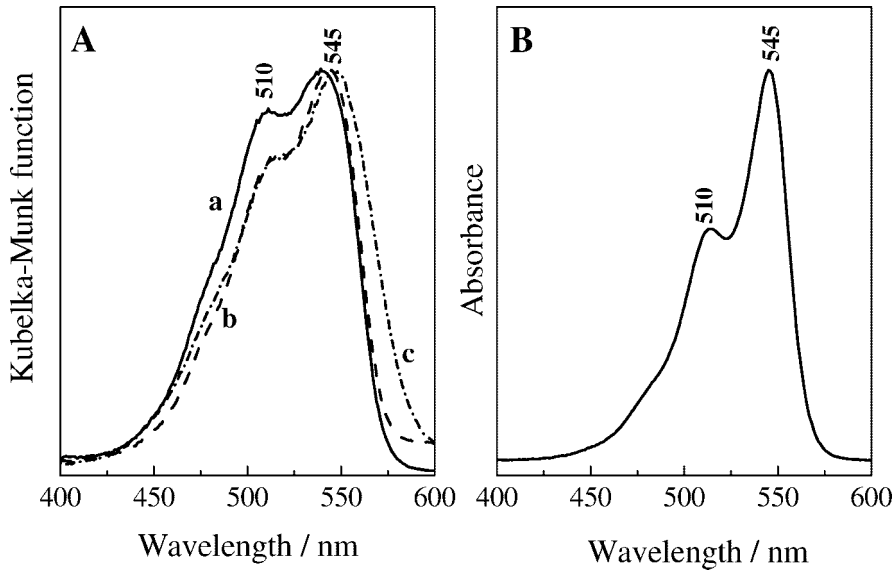

FIGURE 4. (A) DR UV−vis spectra of IRIS3(1)/MCM-41 (curve a), IRIS3(10)/MCM-41 (curve b), and IRIS3(100)/MCM-41 (curve c). (B) UV−vis spectrum of IRIS3 in methanol.

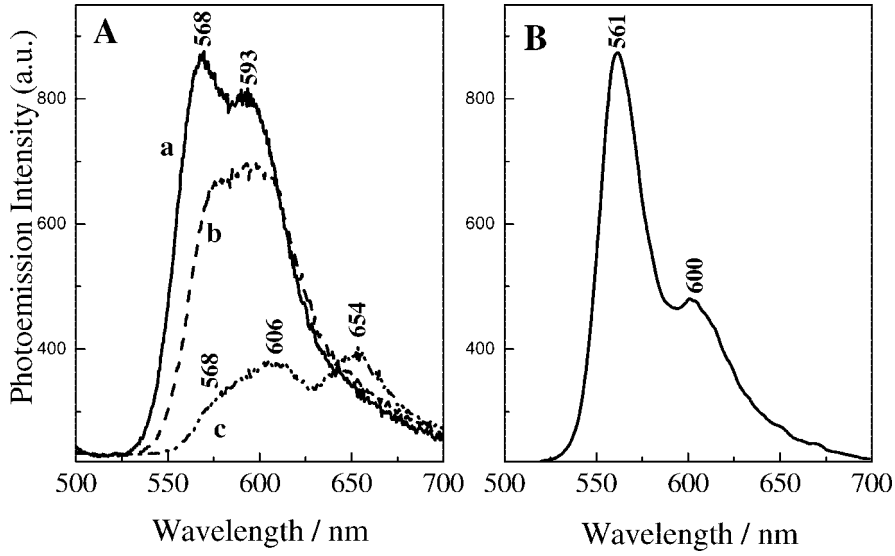

FIGURE 5. (A) Photoluminescence spectra of IRIS3(1)/MCM-41 (curve a), IRIS3(10)/MCM-41 (curve b), and IRIS3(100)/MCM-41 (curve c). (B) Photoluminescence spectrum of IRIS3 in methanol. All of the samples were excited at 480 nm.

rated from it (17). A similar behavior was observed for cyanine aggregates in silica matrixes (16).

The photoluminescence properties of as-prepared hybrids were characterized by emission spectroscopy. The photoemission spectra of IRIS3 embedded within MCM-41 are shown in Figure 5A, at the actual intensity. In this case, the intensities of emission by the hybrids are immediately comparable. For comparison, an emission spectrum of IRIS3 in methanol is given (Figure 5B). All samples were excited at 545 nm, at 510 nm, and in correspondence with the shoulder at 480 nm. The shape of the emission profile is not modified by a change in the excitation wavelength, yet the intensity decreases with a decrease in the excitation wavelength. However, excitation light was fixed at 480 nm to allow a direct comparison of the emission intensity; an excitation wavelength closer to the absorption maximum would require the introduction of attenuator filters for the samples at higher dye loading.

The dye solution (Figure 5B) shows two well-resolved photoemission bands at 561 (intense) and 600 nm (weak). In the case of the low-loading hybrid [IRIS3(1)/MCM-41], the emission spectrum (Figure 5A, curve a) is broadened with respect to the one in solution, indicating that the adsorption of dyes on the inner surface of MCM-41 produces a number of slightly different species (41). With increasing IRIS3 loading (curves b and c), an increase of self-quenching of the emission intensity is observed and the emission profile undergoes a progressive modification. In particular, the two main emission bands at 568 and 593 nm, shown by IRIS3(1)/MCM-41 (curve a), are red shifted with respect to the spectrum of the dye solution, and their relative intensities are changed. These modifications are more evident in IRIS3(10)/MCM-41 (curve b) and IRIS3(100)/MCM-41 (curve c) emission spectra. In the case of a high dye loading sample [IRIS3(100)/MCM-41, curve c], the intensity of the photoemission bands is very low because of the concentration

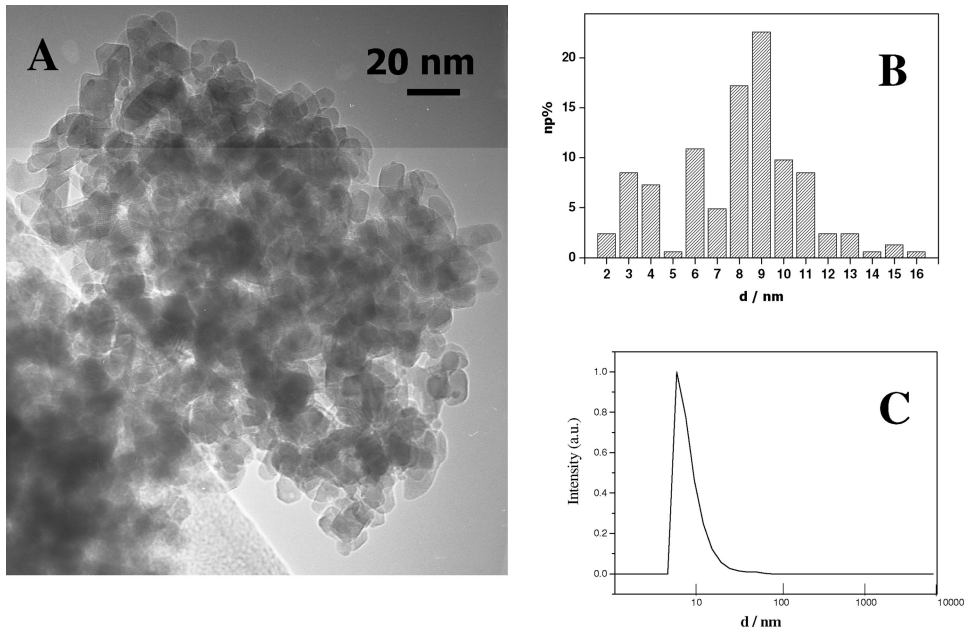

FIGURE 6. (A) HRTEM micrograph of IRIS3(1)/MCM-41 NPs. (B) Particle size distribution of hybrid NPs, calculated by counting ca. 300 particles in HRTEM micrographs. (C) Particle size distribution determined by dynamic light scattering analysis in aqueous media.

quenching effect and a new weak signal at 654 nm is present. This latter signal may be due to an incipient formation of *J*-aggregates, which are not detectable by DR UV−vis because of the lower sensitivity of the technique.

Photoemission data evidenced that the hybrid with the lower dye loading [IRIS3(1)/MCM-41] shows better performance in terms of dispersion of the dye into the channels of MCM-41; this feature is extremely important for further application in the field of Life Science as luminescent probes.

An assessment of the dye distribution in the IRIS3(1)/MCM-41 hybrid was made based on fluorescence lifetime measurements. TCSPC measurements of IRIS3(1)/MCM-41 were recorded. The decay curves for each band were well-fitted by mono- and biexponential decay functions. Fluorescence lifetimes of the hybrid [IRIS3(1)/MCM-41] showed biexponential decay: 70% of the species has a lifetime of 2.6 ns, and 30% has a lifetime close to that of the LED source limit of 0.8 ns ($\chi^2 = 1.1$). The two lifetimes are designated as τ_1 (long) and τ_2 (short). This suggests the presence of two different silica microenvironments around the dye molecules. In particular, it can be hypothesized that the longer lifetime could be assigned to dye molecules surrounded by silanols inside the pores that are much more constrained, while the shorter lifetime could be due to dyes surrounded by silanols present on the external silica surface. Moreover, the τ values of the hybrid materials are longer than those in solution, where cyanine dyes usually show a monoexponential lifetime of about 0.2 ns (33−35). This is due to the high dispersion of dye molecules into the channels of MCM-41, which reduces the IRIS3 intermolecular collisions and the dye−solvent interactions, extending the fluorescence lifetime of the cyanine (41).

3.2. Characterization of Hybrid NPs. TEM analysis has evidenced that the as-prepared hybrid material [IRIS3(1)/MCM-41] is formed by aggregates with a diameter in the 100−300 nm range. To explore the potential of such a material for "in-cell" bioimaging applications, we attempted to reduce the particle size by ultrasonication. The TEM image, shown in Figure 6A, demonstrates that the treatment increased the monodispersity and reduced the particle size of the as-prepared hybrid. The particle size distribution of the sonicated material was calculated by HRTEM (Figure 6B) and by dynamic light scattering (Figure 6C). These data are in good agreement and show the prevalence of NPs [IRIS3(1)/MCM-41 NPs] with diameters in the range of 8−10 nm.

The photoluminescence properties of these NPs were controlled after the ultrasonication treatment. The optical characterization of photoactive hybrid NPs was performed in an aqueous buffer suspension in order to minimize particle aggregation. The quantum yield of NPs was measured by comparison with a dye solution using $\lambda_{ex} = 480$ nm (42). In Figure 7, the emission spectra of a IRIS3(1)/MCM-41 NP suspension (curve a) and IRIS3 in solution (curve b) are reported. The shape of the emission spectrum of a NP suspension is similar to that of the dye solution. The quantum yield of the photoactive hybrid NPs is double that of the dye solution. This result implies that the photoemission efficiency is enhanced by confinement of the dye within the mesoporous channels due to a high degree of dispersion of cyanines and confirms that this confinement is not affected by sonication. The increase in the quantum yield in the hybrid can also be attributed to an increased rigidity of the dye molecules inside the channels with respect to those in solution. In fact, the dye molecules are not able to rotate as in solution, and nonradiative processes, which always compete with the radiative ones when the dyes are in solution, become less important, producing an enhancement of the emission efficiency. A similar behavior is also observed in cyanine-doped silica NPs (43).

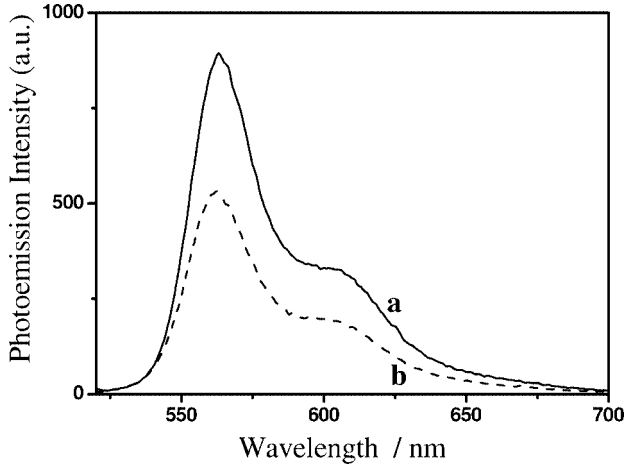

FIGURE 7. Photoluminescence spectra of a IRIS3(1)/MCM-41 NP (curve a) and a IRIS3 solution (curve b).

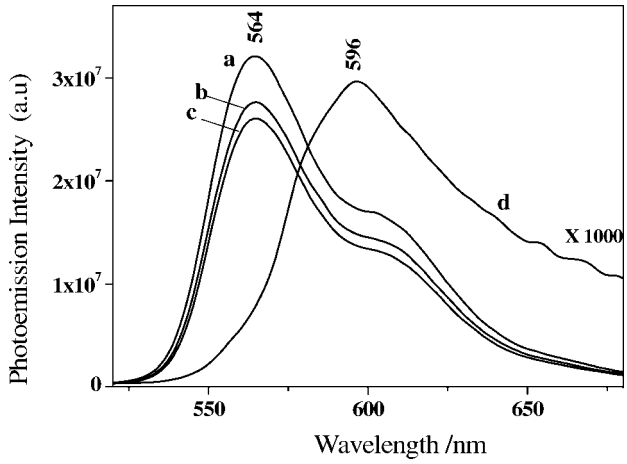

FIGURE 8. Photoluminescence spectra of IRIS3(1)/MCM-41 NPs (λ_{exc} = 510 nm) at different pH values: curve a, pH = 3.6; curve b, pH = 5.50; curve c, pH = 7.4; curve d, pH = 9.

To be employed as reliable fluorescent tracers for intracellular bioimaging, the photoactive NPs should not be affected by pH changes of the cell compartments. For this reason, the photoemission of NPs at different pH values was tested (Figure 8). The NP suspensions in different pH buffers were filtered, and the supernatant was monitored by UV spectroscopy to check for the presence of free dye. This analysis showed no release of cyanine from mesopores incubated in buffers at the pH tested. Light of 510 nm was used to excite NP suspensions incubated in different phosphate buffers. Buffer solutions at pH = 3.60 (curve a), 5.50 (curve b), and 7.40 (curve c) do not modify the emission profile of the NPs because the spectral profiles show a main band at 564 nm with a shoulder at 600 nm typical of the IRIS3 cyanine dye (Figure 5). On the contrary, a very weak emission signal, with a maximum at higher wavelength (596 nm), is observed at pH = 9.00 (curve d). This behavior indicates that the photoactivity of hybrid NPs is irreversibly modified in strongly alkaline conditions.

3.3. Biocompatibility and Photostability of Fluorescent NPs within Intracellular Acid Organelles. One of the main concerns in using NPs to trace biological processes in vivo relies on their tolerability, physicochemical- and photo-stability, and fate. This is of particular relevance when tracing long-term in vivo processes. Cytotoxicity mainly depends on the material, size, and photophysical properties of the NPs because they can leach toxic metals or catalyze the generation of toxic reactive-oxygen free radicals (44−47). The biocompatibility and biodegradability of mesoporous silicas have been tested in various biological systems. In general, silica NPs were shown to be well tolerated in either in vivo or in vitro systems (48, 49). Toxicity was shown to depend on the size and relative concentration of the mesoporous NPs and the time of incubation, as well as on the cell type (50, 51). However, most of these studies have dealt with mesoporous silica NPs of >100 nm in diameter (50−52). Therefore, we assayed the cellular tolerability and the fate of IRIS3(1)/MCM-41 NPs, whose diameter after sonication ranges between 6 and 11 nm (~75%), in several mammal cell lines. In a first set of experiments, we checked the cytotoxicity of IRIS3(1)/MCM-41 by exposing the cells to increasing concentrations of NPs (from 0.01 to 0.05 μg/mL) for up to 24 h and observed no signs of cell death (data not shown). We further investigated the interaction between the NPs and the cells. Mastocyte-like RBL cells (plated on coverslips) were incubated with the NPs (0.01 μg/mL) for up to 24 h, and then the cells were washed twice to remove the excess of NPs passively adsorbed on the cell surface and imaged at different times. Images in Figure 9A show that the IRIS3(1)/MCM-41 NPs rapidly entered the cells and were retained within viable cells, maintaining their fluorescence throughout the incubation period. This indicates that the NPs were not toxic to the cells or degraded or extruded by the cells. A similar result was obtained with human ovary carcinoma cells (Figure 9B), mouse fibroblasts, and neuroblastoma cells (not shown).

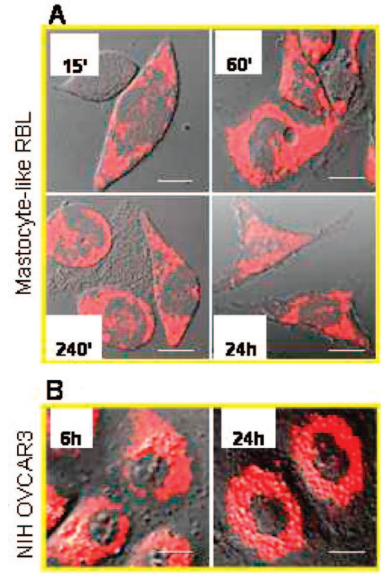

FIGURE 9. Uptake and biocompatibility of IRIS3(1)/MCM-41 NPs. RBL cells (A) and NIH-OVCAR3 cells (B) plated on sterile coverslips were incubated in a medium containing the NPs (0.01 mg/mL for the time indicated). After washing out the excess of noninternalized NPs, the cells were incubated in a fresh medium and imaged at different time points. The images demonstrate that the fluorescent hybrid mesoporous NPs are well tolerated by the cells and retain their fluorescent properties in long-time incubation (bar = 20 μm).

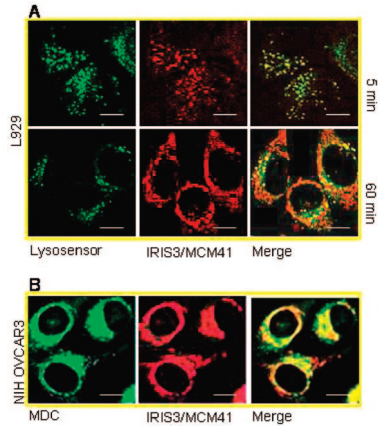

FIGURE 10. (A) L929 fibroblasts incubated with Lysosensor (1 μM; green fluorescence) and the NPs (0.01 mg/mL; red fluorescence) for the time indicated and imaged at the confocal fluorescence microscope. Overlap of the two fluorescence signals demonstrates that NPs enter the cells following the endocytic pathway and accumulate within the same compartments as Lysosensor. Note that in the 60 min incubation vesicles labeled with only IRIS3(1)/MCM-41 NPs are clearly visible, indicating ongoing uptake of the NPs. (B) NIH-OVCAR3 cells incubated for 10 min with IRIS3(1)/MCM-41 NPs (0.01 mg/mL) and MDC (50 μM), washed, and immediately imaged under the fluorescence microscope. Results clearly demonstrate the accumulation of IRIS3(1)/MCM-41 NPs within endosomal−lysosomal compartments.

Cellular uptake of negatively charged silica materials has been shown to occur through nonspecific adsorptive endocytosis (53). To trace the cellular uptake of IRIS3(1)/MCM-41 NPs, L929 mouse fibroblasts were incubated (for 5 and 60 min) with the NPs (0.01 μg/mL) along with Lysosensor (1 μM). The latter traces the endocytic vesicles and eventually accumulates within lysosomes. The images in Figure 10A show that NPs and Lysosensor are taken up by the cells and travel together along the endocytic pathway. By 5 min, Lysosensor is completely endocytosed and has reached its final destination, while NPs continue to be endocytosed so that by 60 min vesicles labeled with only IRIS3(1)/MCM-41 NPs are clearly visible at the periphery of the cell. The endocytic pathway delivers endocytosed material to downstream acid compartments in which the lumenal pH drops to around 5.5 (late endosomes) and 4.0 (lysosomes) (54). These compartments can be labeled by acidotropic fluorophores such as MDC (55). IRIS3(1)/MCM-41 NPs indeed reached these acid compartments as shown by their complete colocalization with MDC in ovary carcinoma cells (Figure 10B).

In a separate study, we have shown that oxidative stress affects the integrity of endosomal and lysosomal compartments of neuroblastoma cells, causing a transient lysosomal membrane permeabilization (i.e., formation of pores) that allows the cytosolic relocation of lysosomal enzymes (37). We asked whether such pores would allow the passage of NPs with a diameter of ~9 nm. SH-SY5Y human neuroblastoma cells were preloaded with IRIS3(1)/MCM-41 NPs (0.01 μg/mL for 15 min) and then exposed or not to 200 μM H_2O_2 for 2 h. In parallel cultures, acid compartments were labeled with AO (1 mg/mL for 5 min), a fluorescent dye that under UV excitation emits a red fluorescence when in the protonated state and a green/yellow fluorescence when not

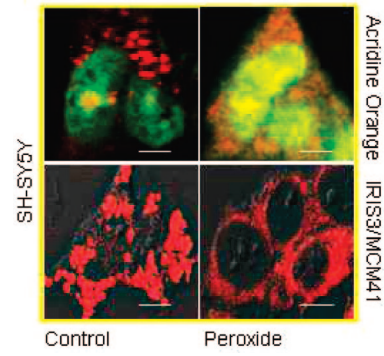

FIGURE 11. IRIS3(1)/MCM-41 NPs that escape the lysosomes following oxidative stress. SH-SY5Y human neuroblastoma cells plated on coverslips were preloaded with the NPs (0.01 mg/mL for 15 min) and then subjected to an acute oxidative stress (200 μM peroxide for 2 h). A parallel set of cells was labeled with AO (1 mg/mL for 5 min) to check the induction of lysosome permeabilization by peroxide. Images demonstrate that the treatment provokes the relocation of NPs from the lysosomes (in control cells) into the cytoplasm (peroxide-treated cells).

protonated (56). Peroxide treatment, in fact, induced the permeabilization of lysosomes, as testified by the leakage of AO (Figure 11). The images in Figure 11 also show that while in control untreated cells the NPs accumulate within lysosomes, in oxidatively stressed cells the NPs relocate and diffuse in the cytosol. This experiment further demonstrates that NPs accumulated in lysosomal organelles and that their dimensions were small enough to allow their passage through the pores provoked by peroxide treatment.

Because the function of endosomal−lysosomal compartments strictly depends on the lumenal acid pH, it was mandatory to check the pH-dependent photostability of NPs in the in vivo system under conditions that disrupt the pH gradient of these compartments. To this end, RBL cells were incubated for 2 h in a fresh medium in the absence or presence of 50 μM CQ, which is known to neutralize the intralysosomal pH (57). Cells were allowed to endocytose the NPs (0.01 μg/mL for 15 min), then the cells were washed, and the fluorescence efficiency of the IRIS3-loaded NPs was assayed under the confocal microscope. To monitor the neutralization of the lysosomal pH induced by CQ, a parallel set of cells was stained with AO. The images in Figure 12 indicate that the IRIS3(1)/MCM-41 NPs retain their ability to trace endosomal−lysosomal organelles even when the intraorganelle pH has been neutralized.

4. CONCLUSIONS

Hybrid materials with promising applications as photoluminescent devices obtained by the encapsulation of cyanine dyes inside MCM-41 mesopores are presented. The inclusion of IRIS3 within the MCM-41 channels has been successfully achieved, as demonstrated by XRD and gas-volumetric analysis. FTIR analysis confirms that IRIS3 dye retains its structural integrity after impregnation. The photoluminescence performances of the IRIS3 dye are preserved within the MCM-41 mesopores. An incipient formation of *J* aggregates occurred at a concentration higher than 10 mg/g [IRIS3(10)/MCM-41], whereas at low dye loading, a uniform distribution of monomeric IRIS3 was achieved.

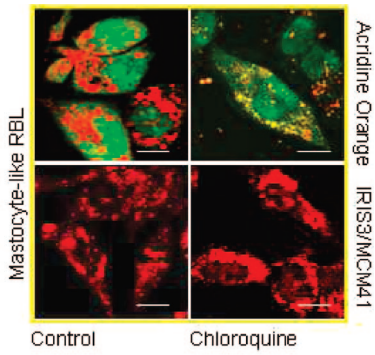

FIGURE 12. IRIS3(1)/MCM-41 NPs that are photostable within acid and neutralized intracellular compartments. RBL cells plated on coverslips were preincubated or not with 50 μM CQ for 2 h. Lysosomal compartments were stained with AO (1 mg/mL for 5 min). Parallel cultures were incubated with IRIS3(1)/MCM-41 NPs (0.01 mg/mL for 15 min). Images were taken at the confocal fluorescence microscope. The result shows that IRIS3(1)/MCM-41 NPs retain their efficient fluorescence within endosomal−lysosomal compartments regardless of their intraluminal pH, either acid in control cells or neutral in CQ-treated cells.

Thus, by tuning of the dye loading in the MCM-41 channels, it is possible to synthesize hybrid materials with different photoluminescence properties, i.e., monomeric species or *J* aggregates. It is reasonable to suppose that the host−guest interaction induces an increased rigidity of the dye structure, as evidenced by photoluminescence spectra. In view of the possible use of these hybrid fluorescent materials for biomedical and biotechnological applications, the hybrid particle sizes were reduced by ultrasonication treatment. The cellular uptake and tolerability, the intracellular compartmentalization, long-term permanence, and photostability within the acid compartments of the IRIS3(1)/MCM-41 NPs were investigated in cultured cells of various origin. Our data indicate that the IRIS3(1)/MCM-41 NPs are well tolerated by mammal cells and are fluorescently stable for a long time. The results support the use of such NPs to trace the vesicular traffic between the endosomal−lysosomal compartments. Moreover, these NPs can be used as platforms for monitoring the delivery of nonsoluble drugs (e.g., antiblastic drugs or enzyme inhibitors) directed to the lysosomes (54).

Acknowledgment. The authors acknowledge financial support by Regione Piemonte (Progetto CIPE 2005 no. D67 and Progetto NANOMAT, Docup 2000−2006, Linea 2.4a and Progetto CIPE 2004 A40 and Ricerca Sanitaria Finalizzata) and by Università del Piemonte Orientale. The authors are also grateful to Compagnia di San Paolo for sponsorship to NIS−Centre of Excellence (Torino, Italy) and to Comoli-Ferrari (Novara, Italy) for sponsorship to the laboratory of Nanobioimaging in Novara.

REFERENCES AND NOTES

(1) Santra, S.; Zhang, P.; Wang, K.; Tapec, R.; Tan, W. *Anal. Chem.* **2001**, *73*, 4988–4993.
(2) Wang, L.; Wang, K.; Santra, S.; Zhao, X.; Hilliard, L. R.; Smith, J. E.; Wu, Y.; Tan, W. *Anal. Chem.* **2006**, *78*, 646–654.
(3) Yan, J.; Estévez, M. C.; Smith, J. E.; Wang, K.; He, X.; Wang, L; Tan, W. *NanoToday* **2007**, *2*, 44–50.
(4) Wu, S.; Zhu, C. *Opt. Mater.* **1999**, *12*, 99–103.
(5) Wirnsberger, G.; Scott, B. J.; Chmelka, B. F.; Stucky, G. D. *Adv. Mater.* **2000**, *12*, 1450–1454.
(6) Fiorilli, S.; Onida, B.; Macquarrie, D.; Garrone, E. *Sens. Actuators, B* **2004**, *100*, 103–106.
(7) Lin, Y. S.; Tsai, C.-P.; Huang, H.-Y.; Kuo, C.-T.; Hung, Y.; Huang, D.-M.; Chen, Y.-C.; Mou, C.-Y. *Chem. Mater.* **2005**, *17*, 4570–4573.
(8) Zhao, W.; Li, D.; He, B.; Zang, J.; Huang, J.; Zang, L. *Dyes Pigm.* **2005**, *64*, 265–270.
(9) Mal, N. K.; Fujiwara, M.; Tanaka, Y. *Nature* **2003**, *421*, 350–353.
(10) Li, D.; Zhang, J.; Anpo, M.; Xue, M.; Liu, Y. *Mater. Lett.* **2005**, *59*, 2120–2123.
(11) Gu, G.; Ong, P. P.; Li, Q. *J. Phys. D: Appl. Phys.* **1999**, *32*, 2287–2289.
(12) Yao, Y.; Zhang, M.; Shi, J.; Gong, M.; Zhang, H.; Yang, Y. *Mater. Lett.* **2001**, *48*, 44–48.
(13) Xu, W.; Guo, H.; Akins, D. L. *J. Phys. Chem. B* **2001**, *105*, 1543–1546.
(14) Seçkin, T.; Gültek, A.; Süleyman, K. *Dyes Pigm.* **2003**, *56*, 51–57.
(15) Xu, W.; Aydin, M.; Zakia, S.; Akins, D. L. *J. Phys. Chem. B* **2004**, *10*, 5588–5593.
(16) Xu, W.; Guo, H.; Akins, D. L. *J. Phys. Chem. B* **2001**, *105*, 7686–7689.
(17) Xu, W.; Akins, D. L. *J. Phys. Chem. B* **2002**, *106*, 1991–1994.
(18) Liu, C. M.; Tung, K. H.; Chang, T. H.; Chien, C. C.; Yen, M. H. *J. Chromatogr., B: Anal. Technol. Biomed. Life Sci.* **2003**, *791*, 315–321.
(19) Mujumdar, S. R.; Mujumdar, R. B.; Charsetta, M. G.; Waggoner, A. S. *Bioconjugate Chem.* **1996**, *7*, 356–362.
(20) Weissleder, R. *Nat. Biotechnol.* **2001**, *19*, 316–317.
(21) Bertolino, C. A.; Caputo, G.; Barolo, C.; Viscardi, G.; Coluccia, S. *J. Fluoresc.* **2006**, *16*, 221–225.
(22) Caputo, G.; Della Ciana, L. New fluorescent cyanine labels containing a sulfamido linker arm. EP 1065250, 1999.
(23) Caputo, G.; Della Ciana, L. Symmetric, monofunctionalised polymethine dyes labelling reagents. EP 1223197, 2001.
(24) Caputo, G.; Della Ciana, L. Process and method for the preparation of asymmetric monofunctionalised indocyanine labelling reagents and obtained compounds. U.S. Patent 0,065,421, 2002.
(25) Bertolino, C. A.; Ferrari, A. M.; Barolo, C.; Viscardi, G.; Caputo, G.; Coluccia, S. *Chem. Phys.* **2006**, *330*, 52–59.
(26) Bujdák, J.; Iyi, N.; Fujita, T. *Colloids Surf., A* **2002**, *207*, 207–214.
(27) Balas, F.; Manzano, M.; Horcajada, P.; Vallet-Regi, M. *J. Am. Chem. Soc.* **2006**, *128*, 8116–8117.
(28) Mal, N. K.; Fujiwara, M.; Tanaka, Y. *Nature* **2003**, *421*, 350–353.
(29) Liong, M.; Lu, J.; Kovochich, M.; Xia, T.; Ruehm, S. G.; Nel, A. E.; Tamanoi, F.; Zink, J. I. *ACS Nano* **2008**, *2*, 889–896.
(30) Song, S. W.; Hidajat, K.; Kawi, S. *Chem. Commun.* **2007**, *42*, 4396–4398.
(31) Hamer, F. M. In *Chemistry of Heterocyclic Compounds*; Weissberger, A., Taylor, E. C., Eds.; Springer: New York, 1964; p 790.
(32) Mori, T.; Kuroda, Y.; Yoshikawa, Y.; Nagao, M.; Kittaka, S. *Langmuir* **2002**, *18*, 1595–1603.
(33) Brismar, H.; Trepte, O.; Ulfhake, B. *J. Histochem. Cytochem.* **1995**, *43*, 699–707.
(34) Kabatc, J.; Piertrzak, M.; Paçzkowski, J. *J. Chem. Soc., Perkin Trans.* **2002**, *2*, 287–295.
(35) Oiwa, K.; Jameson, D. M.; Croney, J. C.; Davis, C. T.; Eccleston, J. F.; Anson, M. *Biophys. J.* **2003**, *84*, 634–642.
(36) Dragonetti, A.; Baldassarre, M.; Castino, R.; Démoz, M.; Luini, A.; Buccione, R.; Isidoro, C. *J. Cell Sci.* **2000**, *113*, 3289–3298.
(37) Castino, R.; Bellio, N.; Nicotra, G.; Follo, C.; Trincher, N. F.; Isidoro, C. *Free Radicals Biol. Med.* **2007**, *42*, 1305–1316.
(38) Castino, R.; Peracchio, C.; Salini, A.; Nicotra, G.; Trincheri, N. F.; Démoz, M.; Valente, G.; Isidoro, C. *J. Cell Mol. Med.* **2008**, "Postprint"; 10.1111/j.1582-4934.00435.x.
(39) Kresge, C. T.; Leonowicz, M. E.; Roth, W. J.; Vartuli, J. C. *Nature* **1992**, *359*, 710–712.
(40) Pardal, A. C.; Ramos, S. S.; Santos, P. F.; Reis, L. V.; Almeida, P. *Molecules* **2002**, *7*, 320–330.
(41) Wang, L.; Shao, J.; Zang, J.; Anpo, M. *Opt. Mater.* **2006**, *28*, 1232–1234.
(42) Ramazzo, E.; Bonacchi, S.; Montalti, M.; Prodi, L.; Zaccheroni, N. *J. Am. Chem. Soc.* **2007**, *129*, 14251–14256.
(43) Alberto, G.; Miletto, I.; Viscardi, G.; Caputo, G.; Coluccia, S.; Martra, G. *J. Phys. Chem. C*, in preparation.
(44) Donaldson, K.; Stone, V.; Tran, C. L.; Kreyling, W.; Borm, P. J. *Occup. Environ. Med.* **2004**, *61*, 727–728.

(45) Wilson, M. R.; Lightbody, J. H.; Donaldson, K.; Sales, J.; Stone, V. *Toxicol. Appl. Pharmacol.* **2002**, *184*, 172–179.
(46) Dick, C. A.; Brown, D. M.; Donaldson, K.; Stone, V. *Inhalation Toxicol.* **2003**, *15*, 39–52.
(47) Derfus, A. M.; Chan, W. C. W.; Bathia, S. N. *Nano Lett.* **2004**, *4*, 11–18.
(48) Li, X.; Zhang, L. X.; Dong, X. P.; Liang, J.; Shi, J. *Microporous Mesoporous Mater.* **2007**, *102*, 151–158.
(49) Radin, S.; El-Bassyouni, G.; Vresilovic, E. J.; Schepers, E.; Ducheyne, P. *Biomaterials* **2005**, *26*, 1043–1052.
(50) Hudson, S. P.; Padera, R. F.; Langer, R.; Kohane, D. S. *Biomaterials* **2008**, *29*, 4045–4055.
(51) Valhov, H.; Gabrielsson, S.; Strømme, M.; Scheynius, A.; Garcia-Bennet, A. E. *Nano Lett.* **2007**, *7*, 3576–82.
(52) Lu, J.; Liong, M.; Zink, J. I.; Tamanoi, F. *Small* **2007**, *3*, 1341–6.
(53) Xing, X. L.; He, X. X.; Peng, J. F.; Wang, K.; Tan, W. *J. Nanosci. Nanotechnol.* **2005**, *5*, 1688–1693.
(54) Castino, R.; Démoz, M.; Isidoro, C. *J. Mol. Recognit.* **2003**, *16*, 337–348.
(55) Castino, R.; Isidoro, C.; Murphy, D. *FASEB J.* **2005**, *19*, 1024–1026.
(56) Canonico, P. G.; Bird, J. W. *J. Cell. Biol.* **1969**, *43*, 367–371.
(57) Isidoro, C.; De Stefanis, D.; Démoz, M.; Ogier-Denis, E.; Codogno, P.; Baccino, F. M. *Cell Growth Differ.* **1997**, *8*, 1029–1037.

AM800196R